THE WEAKLY NONLINEAR MAGNETOROTATIONAL INSTABILITY IN A THIN-GAP TAYLOR-COUETTE FLOW

S. E. Clark[1] and Jeffrey S. Oishi[2,3]
Draft version October 5, 2016

ABSTRACT

The magnetorotational instability (MRI) is a fundamental process of accretion disk physics, but its saturation mechanism remains poorly understood despite considerable theoretical and computational effort. We present a multiple-scales analysis of the non-ideal MRI in the weakly nonlinear regime – that is, when the the most unstable MRI mode has a growth rate asymptotically approaching zero from above. Here, we develop our theory in a thin-gap, Cartesian channel. Our results confirm the finding by Umurhan et al. (2007) that the perturbation amplitude follows a Ginzburg-Landau equation. We extend these results by performing a detailed force balance for the saturated azimuthal velocity and vertical magnetic field, demonstrating that even when diffusive effects are important, the bulk flow saturates via the combined processes of reducing the background shear and rearranging and strengthening the background vertical magnetic field. We directly simulate the Ginzburg-Landau amplitude evolution for our system and demonstrate the pattern formation our model predicts on long length and time scales.

1. INTRODUCTION

For matter to accrete from a disk onto a central object, angular momentum must be transported radially outward in the disk. The transport mechanism is likely turbulent, as molecular viscosity alone cannot account for the needed angular momentum transfer, and likely magnetic, as this turbulence is excited even in hydrodynamically stable disks (Shakura & Sunyaev 1973). Discovered by Chandrasekhar (1960) and Velikhov (1959) in a global geometry, the magnetorotational instability (MRI) was subsequently rediscovered and applied to accretion disks by Balbus & Hawley (1991). Since then, the MRI remains the leading explanation for rapid angular momentum transport in astrophysical disks. The instability in its simplest geometry arises when a differentially rotating disk is threaded by a vertical magnetic field. The presence of the magnetic field linearly destabilizes the disk gas, driving turbulence and angular momentum transport (e.g. Hawley et al. 2011; Parkin 2014; Parkin & Bicknell 2013). The MRI likely plays a role in a diverse host of astrophysical systems, including protoplanetary disks (e.g. Bai 2015) and black hole accretion disks (e.g. Schnittman et al. 2013), as well as stellar interiors (e.g. Wheeler et al. 2015). Despite its importance, many aspects of the MRI remain poorly understood. In particular, the nonlinear saturation mechanism for the MRI is an open question, and a formidable challenge. MRI saturation has been tackled almost exclusively with simulation, with a few notable exceptions detailed below. In this work we analytically investigate the weakly nonlinear saturation of the MRI.

Weakly nonlinear analysis is a perturbative method used to examine the asymptotic behavior of a system

near threshold – that is, when the system is just barely unstable to its most unstable mode. The analytical technique follows the multiscale evolution of fluid variables in a perturbation expansion, allowing the controlled interaction of modes between orders in a perturbation series (Bender & Orszag 1978). Weakly nonlinear analysis can be a powerful technique for analytically examining systems which in their full generality exhibit such complicated nonlinear behavior that their study is relegated primarily to the simulation domain. The MRI is one such phenomenon: while there is a rich literature analytically examining the linear MRI, analytical treatments of the *nonlinear* system are relatively few. The weakly nonlinear treatment of the MRI was pioneered by Knobloch & Julien (2005) and Umurhan et al. (2007b, hereafter URM07; see also 2007a). The latter authors undertook the first weakly nonlinear analysis of the MRI in a thin-gap Taylor-Couette (TC) flow with strong dissipation (as is appropriate to liquid metal experiments), and found that the marginal MRI system approaches saturation in a manner analogous to that of Rayleigh-Bénard convection. Weakly nonlinear analysis was instrumental in our understanding of Rayleigh-Bénard convection saturation (Newell & Whitehead 1969), and the similarities between convection and the thin-gap MRI are the result of important shared symmetries between the systems. The success of URM07 in modeling the MRI system near threshold merits further consideration, but we are unaware of any other attempts to expand upon their theoretical framework. In this work we rederive the theory of URM07, and expand upon their findings. Our focus here is on fully characterizing the thin-gap MRI system, both for independent theoretical interest and to have a robust comparison point for extensions of this theory into more complicated geometries. In a companion paper we derive for the first time the weakly nonlinear theory of the standard and helical MRI in a global, cylindrical TC flow (Clark & Oishi 2016b, hereafter Paper II). The thin- and wide-gap treatments complement one another theoretically, and both are important regimes for comparison

[1] Department of Astronomy, Columbia University, New York, NY
[2] Department of Physics and Astronomy, Bates College, Lewiston, ME
[3] Department of Astrophysics, American Museum of Natural History, New York, NY

with simulation.

This work examines TC flow in the thin-gap regime, an idealization in which the radial extent of the channel is very small compared to its distance from the center of rotation, i.e. $(r_2 - r_1) \ll \frac{1}{2}(r_1 + r_2)$ where r_1 and r_2 are the radii of the inner and outer flow boundaries, respectively. The thin-gap approximation eliminates curvature terms, so the domain geometry is Cartesian rather than cylindrical. The excluded curvature terms have an explicit dependence on r, so they make the problem more challenging both analytically and numerically. In particular, in the wide-gap geometry (i.e. true Taylor-Couette flow) the base angular velocity is a function of r, where in the thin-gap approximation the shear flow reduces to a linear profile.

We note several other important analytical studies of MRI saturation. Knobloch & Julien (2005) analyze the MRI in the strongly nonlinear regime, by following the already-developed MRI modes into asymptotic saturation. They consider a thin-gap regime as well, and so their theory may be considered the strongly nonlinear analogue to the one developed here. Vasil 2015 examines the weakly nonlinear MRI in a thin-gap regime in a minimal model, finding deep mathematical similarities between the MRI system and the elastodynamic instability of a buckling beam. We discuss these results and their relation to ours in section 4. Several authors have investigated the behavior of the MRI when the boundary conditions are shear periodic, and so the MRI has no mechanism by which to modify the background shear flow profile. In this approximation linear MRI growth is dominated by channel modes, a type of MRI mode that, for periodic boundary conditions, are exact solutions of both the linear and nonlinear MRI equations (Goodman & Xu 1994). In this regime the MRI saturates via parasitic instabilities, which feed off and destroy the primary MRI modes. Analytical investigation of this case reveals that MRI saturation can be caused by parasitic Kelvin-Helmholtz and tearing mode instabilities, depending on parameter regime (Pessah 2010). The theory of MRI channel mode parasites is robust (see also Pessah & Goodman 2009, Latter et al. 2010, Rembiasz et al. 2016), but their importance may be overestimated by the local approximation (Latter et al. 2015), and not germane to global analyses like the one presented here. Latter et al. (2015) gives a detailed analysis of the relation between local and global linear MRI modes.

We begin with an overview of our basic model equations for the thin gap MRI in section 2 and then describe our weakly non-linear analysis and give basic results in section 3. We then place our results in the ocntext of previous results from both analytic and computational studies in section 4 and draw conclusions in section 5.

2. EQUATIONS

The evolution of a conducting fluid is governed by the momentum and induction equations,

$$\partial_t \mathbf{u} + \mathbf{u} \cdot \nabla \mathbf{u} = -\frac{1}{\rho}\nabla P - \nabla \Phi + \frac{1}{\rho}(\mathbf{J} \times \mathbf{B}) \qquad (1)$$
$$+ \nu \nabla^2 \mathbf{u} - 2\mathbf{\Omega} \times \mathbf{u} - \mathbf{\Omega} \times (\mathbf{\Omega} \times \mathbf{r}),$$

$$\partial_t \mathbf{B} = \nabla \times (\mathbf{u} \times \mathbf{B}) + \eta \nabla^2 \mathbf{B}, \qquad (2)$$
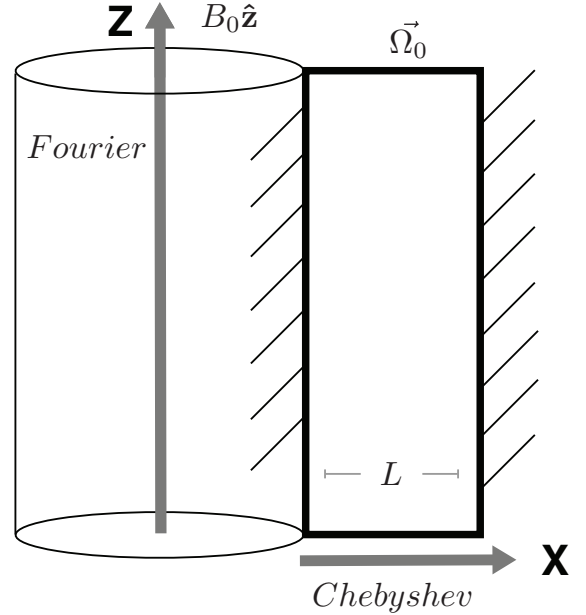

Fig. 1.— Schematic diagram of our set-up, an axisymmetric thin-gap Taylor-Couette flow. We investigate a 2D slice of the X-Z (radial-vertical) plane. Our domain is represented by the bolded black box, of width L. The radial dimension is solved with a basis of Chebyshev polynomials, and the vertical dimension is solved on a Fourier basis.

where P is the gas pressure, ν is the kinematic viscosity, η is the microscopic diffusivity, $\nabla\Phi$ is the gravitational force per unit mass, and the current density is $\mathbf{J} = \nabla \times \mathbf{B}$. Equations 1 and 2 are subject to the incompressibility and magnetic solenoid constraints,

$$\nabla \cdot \mathbf{u} = 0 \qquad (3)$$

$$\nabla \cdot \mathbf{B} = 0. \qquad (4)$$

We axisymmetrically perturb all three vector components of each of the fluid quantities. We nondimensionalize the equations, with lengths nondimensionalized by L, time by Ω_0, velocities by $\Omega_0 L$, magnetic fields by B_0, and pressure by $\Omega_0^2 L^2 \rho_0$, where L is the channel width, Ω_0 is the rotation rate at the center of the channel, and ρ_0 is the constant pressure in the base state (see Figure 1). We define the Reynolds number, $\mathrm{Re} \equiv \Omega_0 L^2/\nu$, magnetic Reynolds number, $\mathrm{Rm} \equiv \Omega_0 L^2/\eta$, and a plasma beta parameter, $\beta \equiv \Omega_0^2 r_0^2/v_A^2$, where the Alfvén speed v_A is $v_A^2 = B_0^2/\rho_0$. The fluid symbols $\mathbf{u}$, $\mathbf{B}$, etc. will henceforth be used to refer to the nondimensional, perturbed quantities.

We define the streamfunction Ψ and flux function A, where A is the familiar two-dimensional vector potential. Ψ and A are scalar fields. The curl of Ψ and the curl of A are defined as the velocity and magnetic field perturbation, respectively, and so Ψ and A automatically satisfy our constraints (Equations 3 and 4).

Ψ and A are thus related to the velocity and magnetic

field perturbations, respectively, as

$$\mathbf{u} = \begin{bmatrix} \partial_z \Psi \\ u_y \\ -\partial_x \Psi \end{bmatrix}, \qquad (5)$$

$$\mathbf{B} = \begin{bmatrix} \partial_z A \\ B_y \\ -\partial_x A \end{bmatrix}. \qquad (6)$$

Our final equation set is

$$\partial_t \nabla^2 \Psi + J\left(\Psi, \nabla^2 \Psi\right) - 2\partial_z u_y = \\ \frac{2}{\beta} B_0 \partial_z \nabla^2 A + \frac{2}{\beta} J\left(A, \nabla^2 A\right) + \frac{1}{\mathrm{Re}} \nabla^4 \Psi \quad (7)$$

$$\partial_t u_y + J\left(\Psi, u_y\right) + (2-q)\,\Omega_0 \partial_z \Psi = \\ \frac{2}{\beta} B_0 \partial_z B_y + \frac{2}{\beta} J\left(A, B_y\right) + \frac{1}{\mathrm{Re}} \nabla^2 u_y \quad (8)$$

$$\partial_t A = B_0 \partial_z \Psi + J\left(A, \Psi\right) + \frac{1}{\mathrm{Rm}} \nabla^2 A \quad (9)$$

$$\partial_t B_y = B_0 \partial_z u_y + J\left(A, u_y\right) - J\left(\Psi, B_y\right) \\ + \frac{1}{\mathrm{Rm}} \nabla^2 B_y - q\Omega_0 \partial_z A, \quad (10)$$

where J is the Jacobian operator,

$$J\left(f, g\right) \equiv \partial_z f \partial_x g - \partial_x f \partial_z g, \qquad (11)$$

and $q \equiv -d \ln \Omega / \ln R = 3/2$ is the dimensionless shear parameter defining a rotation profile $\Omega(r) = \Omega_0(r/r_0)^{-q}$, such that the background velocity profile is $u_0 = -q\Omega_0 x$.

The weakly nonlinear regime is where the MRI system is nonlinearly unstable to only the most unstable mode of the linear solution. We find the marginal state, where the most unstable linear MRI mode neither grows nor decays, for a set of dimensionless parameters, and then destabilize the system.

Because we nondimensionalize B by the magnitude of the background field strength, $B_0 \equiv 1$ in Equations 7 - 10. To excite the weakly nonlinear MRI, we tune the background magnetic field down away from stability (recall that stronger vertical fields stabilize the MRI). We do so by substituting $B = B_0\left(1 - \epsilon^2\right)$. The degree of departure from the marginal state is measured by the small parameter ϵ. An $\mathcal{O}\left(\epsilon^2\right)$ weakening of the background magnetic field destabilizes a finite band of wave modes with a width of $\mathcal{O}\left(\epsilon\right)$, which interact nonlinearly.

The destabilizing substitution is made, and Equations 7 - 10 are rewritten such that the fluid variables are contained in a state vector

$$\mathbf{V} = \left[\Psi, u_y, A, B_y\right]^{\mathrm{T}}. \qquad (12)$$

This yields the system of equations

$$\mathcal{D}\partial_t \mathbf{V} + \mathcal{L}\mathbf{V} + \epsilon^2 \widetilde{\mathcal{G}} = \mathbf{N}, \qquad (13)$$

where we leave the definition of the matrices $\mathcal{D}$, $\mathcal{L}$, and $\widetilde{\mathcal{G}}$ to Appendix A, and the detailed form of the nonlinear

vector $\mathbf{N}$ to Appendix B. We solve this system subject to no-slip, perfectly conducting radial boundary conditions, defined as

$$\Psi = \partial_x \Psi = u_y = A = \partial_x B_y = 0. \qquad (14)$$

3. WEAKLY NONLINEAR ANALYSIS

We conduct a formal multiple scales analysis of this system. Our perturbations are characterized in terms of fast- and slow-moving variables, that we treat as independent in order to simultaneously track the evolution of the system on two scales. The relative scalings of the fast and slow variables are chosen such that each of the temporal and spatial eigenvalues appear at the same lowest order in the linear dispersion relation (Appendix C). The scalings are

$$X \equiv \epsilon x, \ Y \equiv \epsilon y, \ Z \equiv \epsilon z, \ T \equiv \epsilon^2 t. \qquad (15)$$

Note that these are the same scalings as apply to Rayleigh-Bénard convection and hydrodynamic TC flow. Our x dimension, the direction of angular momentum transport, is analogous to the direction of temperature transport in the convection problem. In analogy to these problems, we posit slow variation in both Z and T. Each operator in Equations 7 - 10 is expanded to reflect these scalings – for instance, ∂_z becomes $\partial_z + \epsilon \partial_Z$.

The multiple scale dependencies of our solution are encoded into an ansatz for the linear MRI solution at marginality,

$$\mathbf{V_1} = \alpha(T, Z)\mathbb{V}_{11}(x)e^{ik_c z} + c.c. + \beta(T, Z)\mathbb{U}_{11}(x) \quad (16)$$

where α is a slowly-varying amplitude equation and $c.c.$ denotes the complex conjugate. The x dependence is contained in $\mathbb{V}_{11} = (\Psi_{11}, u_{11}, A_{11}, B_{11})^{\mathrm{T}}$, and must be solved subject to the radial boundary conditions. The periodic vertical boundary conditions allow us to posit the z dependence, where k_c is the value of the vertical wavenumber at marginality. As noted by URM07, there exists a spatially constant neutral mode solution to the B_y equation, with $\mathbb{U}_{11} = (0, 0, 0, 1)^{\mathrm{T}}$. The amplitude $\beta(T, Z)$ encodes the slow evolution of this mode.

The state vector is expanded in a perturbation series in orders of ϵ,

$$\mathbf{V} = \epsilon \mathbf{V_1} + \epsilon^2 \mathbf{V_2} + \epsilon^3 \mathbf{V_3} + h.o.t. \qquad (17)$$

Our perturbed system is then expressed order by order as

$$\mathcal{O}(\epsilon) : \mathcal{L}\mathbf{V_1} + \mathcal{D}\partial_t \mathbf{V_1} = 0. \qquad (18)$$

$$\mathcal{O}(\epsilon^2) : \mathcal{L}\mathbf{V_2} + \widetilde{\mathcal{L}}_1 \partial_Z \mathbf{V_1} = \mathbf{N_2} \qquad (19)$$

$$\mathcal{O}(\epsilon^3) : \mathcal{L}\mathbf{V_3} + \mathcal{D}\partial_T \mathbf{V_1} + \widetilde{\mathcal{L}}_1 \partial_Z \mathbf{V_2} + \widetilde{\mathcal{L}}_2 \partial_Z^2 \mathbf{V_1} + \widetilde{\mathcal{G}}\mathbf{V_1} = \mathbf{N_3} \qquad (20)$$

The partial differential equations that comprise Equations 18 to 20 are solved in succession. The practical advantage of our ansatz construction (Equation 16) is clear: the separable x-dependence means that the radial boundary conditions are solved in only one dimension. Thus our analytical framework is able to side-step many
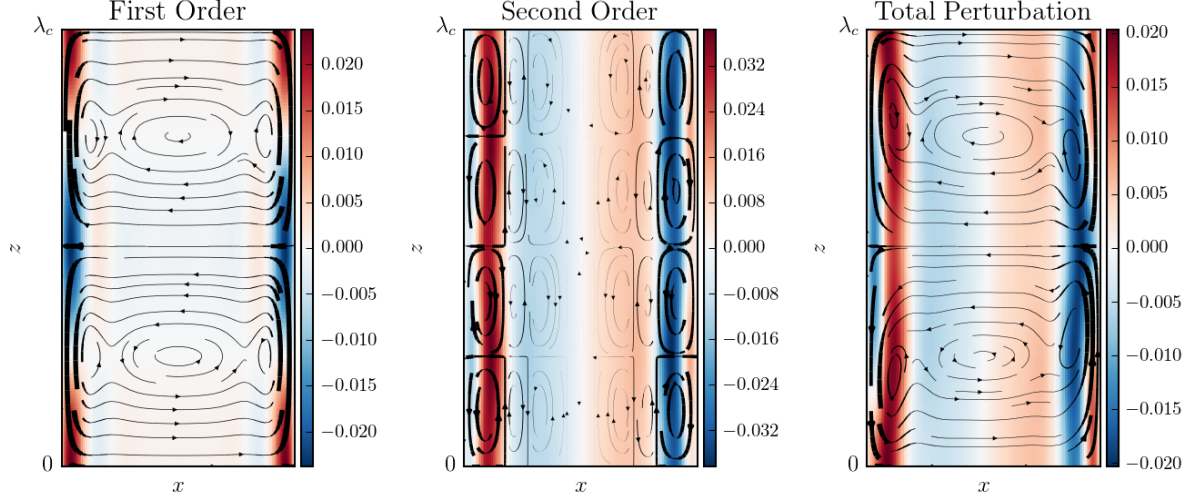
FIG. 2.— First order (left), second order (center), and total (right) velocity perturbations. Streamlines represent velocity in the vertical-radial plane, where thicker streamlines correspond to faster speeds. Colorbar represents azimuthal velocity. We use a constant amplitude $\alpha = \alpha_{saturation}$ and a small parameter $\epsilon = 0.5$.
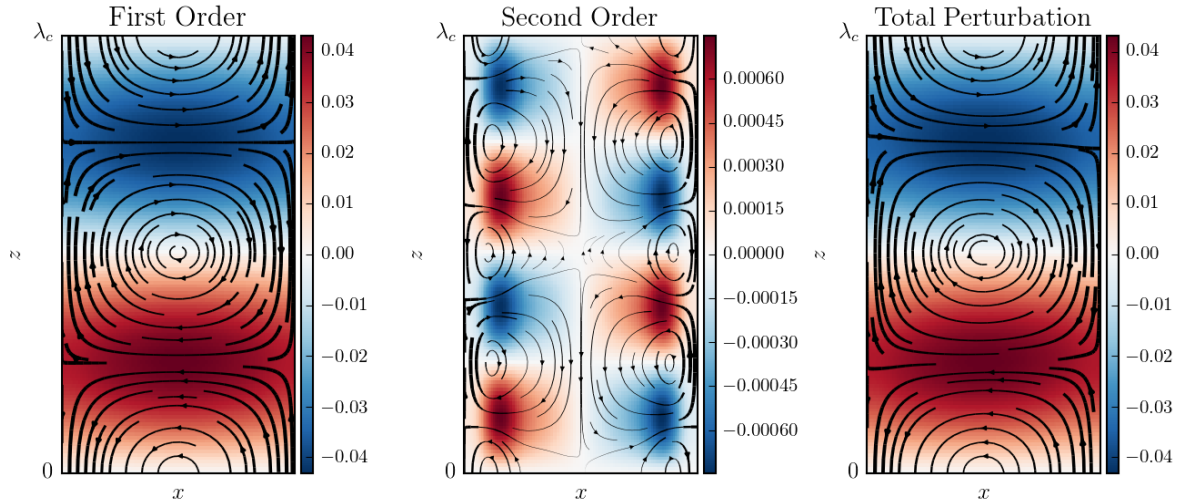

FIG. 3.— As in Figure 2 but for the magnetic field. Streamlines represent magnetic field structure in the vertical-radial plane, where thicker streamlines correspond to higher magnetic field strengths. Colorbar represents azimuthal magnetic field strength.

of the resolution issues faced by multidimensional simulations. We are able to resolve even small-scale structure in the boundary layers of our domain, because we need only resolve it in one dimension. We solve the radial component of each equation using the open source pseudospectral code Dedalus. We compute the radial components on a grid of Chebyshev polynomials, as is appropriate for bounded one-dimensional domains (e.g. Boyd 2001). The nonuniform spacing of the Chebyshev grid allows us to resolve the boundary layers well on a 128-point grid.

To close the perturbation series we enforce a solvability criterion on Equation 20 (see Appendix A). This leads to an amplitude equation for $\alpha(T, Z)$ that governs the slow length- and timescale evolution of the system. This amplitude equation is

$$\partial_T \alpha = b\alpha + h\partial_Z^2 \alpha - c\alpha \left| \alpha^2 \right|, \qquad (21)$$

a real Ginzburg-Landau equation. The saturated solution to Equation 21 is evidently $\alpha_{saturation} = \pm\sqrt{b/c}$. We plot the first order, second order, and total perturbation structure of the fluid variables in Figures 2 and 3 with a constant $\alpha_{saturation}$. This is the Ginzburg-Landau equation that was previously found by URM07. Those authors investigated the behavior of this MRI system as a function of Pm. By analyzing the system over several orders of magnitude in Pm, we reproduce the URM07 result that the analytic saturation amplitude scales as $\alpha_{saturation}^2 \propto \text{Pm}^{4/3}$ in a thin-gap geometry when Pm $\ll$ 1. We also find, as in URM07, that the neutral mode amplitude β is governed by a simple diffusion equation that decouples from the Ginzburg-Landau equation.
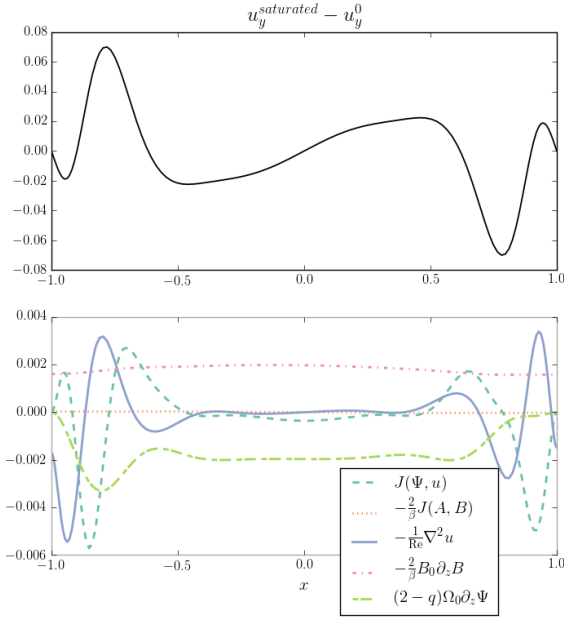
4. DISCUSSION

FIG. 4.— Top panel: Mean radial profile for $u_y^{saturated} - u_y^0$, the difference between the saturated azimuthal velocity profile and the initial azimuthal velocity profile (TC flow). Bottom panel: each term in the steady state force balance (Equation 8 with $\partial_t u_y = 0$). Saturated quantities are computed with $\alpha_{saturation} = \sqrt{b/c}$ and $\epsilon = 0.5$. The saturated state shows reduced shear in the bulk of the flow, outside of the boundary layers.
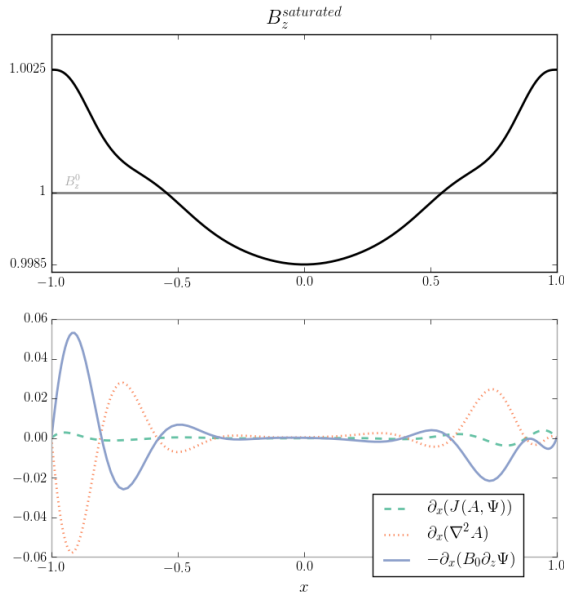

FIG. 5.— Top panel: Mean radial profile for $B_z^{saturated}$, the saturated vertical magnetic field (black line). $B_z^0 = 1$ is the constant background magnetic field (gray line). Bottom panel: each term in the steady state inductive balance (∂_x of Equation 10 with $\partial_t B_y = 0$). Saturated quantities are computed with $\alpha_{saturation} = \sqrt{b/c}$ and $\epsilon = 0.5$. The saturated field is pushed to the radial domain boundaries.

The fact that we find a Ginzburg-Landau equation for the amplitude is unsurprising: such an amplitude equation can be found in any system with Euclidean symmetry and a quadratic maximum in growth rate with respect to the wavenumber (Hoyle 2006). In this case, the Euclidean symmetry comes from axisymmetry in the x-z plane, and the quadratic maximum is a consequence of the linear dispersion relation given in Appendix C. In Paper II, we show that the same symmetry occurs in the axisymmetric global geometry as well.

Here our focus is on a physical description of the saturation mechanism. Figure 4 shows the saturated mean radial profiles of $u_0 - u_y = -q\Omega_0 x - u_y$ and each term in the steady state force balance (i.e. Equation 8 with $\partial_t u_y = 0$). In the bulk of the fluid away from the boundary layers, the saturated state shows reduced shear, with little diffusive contribution. This demonstrates that even in a case where diffusive effects are important, the bulk of the fluid saturates by balancing shear and magnetic tension. As discussed at length in Vasil (2015), when diffusive effects are not important, it is impossible to rearrange momentum without also rearranging the magnetic field. The Vasil (2015) model demonstrates saturation without diffusive effects; our results show that outside of the boundary layers, a simultaneous rearrangement of momentum and field occurs. In the boundary layers, the non-linear advection balances viscous dissipation.

Figure 5 shows B_z and the terms corresponding to steady state inductive balance (∂_x of Equation 10 with $\partial_t B_y = 0$). Here, the instability acts to push magnetic field toward the boundaries in both the bulk and the boundary layers. Note also that the total magnetic energy in the B_z component is significantly larger than the initial condition. Ebrahimi et al. (2009) considered the saturation of a single, strongly super-critical MRI mode allowed to interact non-linearly only with itself and the mean. They considered two important cases, one in which the mean flow was forced to remain at its initial, quasi-Keplerian state for all time, and one in which the background flow was allowed to evolve. This is a crucial difference between the shearing box and our narrow-gap TC flow: perturbations in our simulation can adjust the background flow, whereas in a shearing box, the shear periodicity forbids perturbations from affecting the mean flow. In the case with a freely evolving background flow, Ebrahimi et al. (2009) found a saturated state quite similar to ours: field pushed to the boundaries, and a reduction in shear in the bulk of the flow. Their flows have less pronounced boundary layers, likely because of their much larger Pm = 0.1 − 1.

In the high Re and Rm limit, Vasil (2015) derives an amplitude equation considerably different than the one found here. By averaging in the z direction, the author computes a mean-field equation with striking similarity to the buckling of an elastic beam under load. The most salient feature of this equation is its *non-local* character. Unlike the present work, which focuses on Keplerian rotation profiles with $q = 3/2$ with a critical background magnetic field strength, Vasil (2015) focuses on a fixed field strength and a weakly destabilized shear profile. These differences are minor, however: the destabilizing parameter ϵ enters the analysis in the same quadratic proportion. Whether and how Vasil (2015)'s amplitude equation is equivalent to our own in the limit of dynam-

FIG. 6.— Evolution of the Ginzburg-Landau amplitude equation (Equation 21) on a Fourier Z domain of length $2\lambda_{crit}$, where $\lambda_{crit} = 2\pi/k_c$ is the critical wavelength of the system. Top left panel shows the evolution of the amplitude observable $\alpha\alpha^*$ on the full Z domain as a function of time T. Bottom left panel shows the amplitude *alpha* at the final timestep shown, where the black line is the real part $\mathrm{Re}\{\alpha(t = t_{final})\}$ and the gray line is the imaginary part $\mathrm{Im}\{\alpha(t = t_{final})\}$. The final amplitude is bounded by the analytic saturation amplitude $\alpha_{saturation} = \pm\sqrt{b/c}$. Top right panel shows the evolution of the phase angle $\phi = \arctan(\mathrm{Im}(\alpha)/\mathrm{Re}(\alpha))$ on the same domain. Bottom panel shows the phase angle as a function of Z for the final timestep. Note that the phase angle is wrapped on a 2π domain, such that $\pi = -\pi$, as indicated by the circular colorbar.

FIG. 7.— As in Figure 6 but for a Z domain of length $10\lambda_{crit}$.

ically important resistive and viscous effects is beyond the scope of this work. Nevertheless, the author identifies the non-linear term responsible for saturation as consisting of flux and field transport and notes these are the only mechanisms able to produce saturation. Our results likewise demonstrate a combination of flux and field transport in the comparable region of our domain. This suggests that despite our formulation displaying different saturation dynamics (Ginzburg-Landau in our case; a network of coupled Duffing oscillators in Vasil 2015), there may indeed be an underlying unification.

The real Ginzburg-Landau equation describes the amplitude behavior of our system close to threshold. Although the form of the equation is generic to many systems, its coefficients depend on the specific physics of our system and govern its detailed evolution (see Appendix A). We simulate the evolution of the MRI amplitude equation by solving Equation 21 on a Fourier basis in Z using Dedalus. We initialize uniform random noise of amplitude -10^{-3} to $+10^{-3}$ in Z, and timestep the system using a four-stage, fourth-order Runge-Kutta integrator. We evolve the system for $100\Omega_0^{-1}$ in timesteps of $0.02\Omega_0^{-1}$. Results are shown in Figures 6 and 7, where the amplitude and phase structure over the vertical domain is plotted for every 20 timesteps. The system quickly organizes itself into rolls in Z bounded by the analytic saturation amplitude $\alpha_s = \sqrt{b/c}$. The specific geometry depends on the number of critical wavelengths $\lambda_{crit} = 2\pi/k_c$ that are initialized in Z. Figure 6 shows that a system with a height equal to two critical wavelengths will be modulated by simple rolls of sinusoidal amplitude. The saturation amplitude pattern becomes more complicated when more modes are allowed to interact. Figure 7 shows the evolution of a system of height $10\lambda_{crit}$. While still bounded by α_s, the saturation amplitude exhibits a nonlinear phase geometry due to the nonlinear interaction of modes in Z.

5. CONCLUSION

In this paper we construct a weakly nonlinear analysis of the MRI using multiple-scales analysis, leading to a real Ginzburg-Landau equation for the nonlinear amplitude, confirming the previous results of Umurhan et al. (2007b). We also confirm their results for the scaling of the analytic saturation amplitude with Pm. We extend their results by constructing a detailed force and inductive balance for the saturated u_y and B_z components. In doing so, we find the saturated state is a complex balance in which reduction of shear and amplification and redistribution of B_z combine to saturate the instability. We also perform direct numerical simulations of the amplitude equation. We demonstrate that complex patterns can organize the flow on long length scales Z, though the maximum magnitude of the amplitude α is well predicted by the steady state solution. In Paper II, we make use of the techniques developed here to extend the weakly nonlinear analysis of the MRI to a full cylindrical geometry appropriate for a Taylor-Couette experiment.

6. ACKNOWLEDGMENTS

APPENDIX

A. DETAILED EQUATIONS

Here we detail the perturbation analysis described in Section 3. The perturbation series is described by Equations 18 - 20, where

$$\mathcal{L} = \mathcal{L}_0 + \mathcal{L}_1 \partial_z + \mathcal{L}_2 \partial_z^2 + \mathcal{L}_3 \partial_z^3 + \mathcal{L}_4 \partial_z^4, \tag{A1}$$

$$\widetilde{\mathcal{L}}_1 = \mathcal{L}_1 + 2\mathcal{L}_2 \partial_z + 3\mathcal{L}_3 \partial_z^2 + 4\mathcal{L}_4 \partial_z^3 \tag{A2}$$

$$\widetilde{\mathcal{L}}_2 = \mathcal{L}_2 + 3\mathcal{L}_3 \partial_z + 6\mathcal{L}_4 \partial_z^2 \tag{A3}$$

$$\widetilde{\mathcal{G}} = -\mathcal{G} \partial_z - \mathcal{L}_3 \partial_z^3, \tag{A4}$$

and the constituent matrices are defined as

$$\mathcal{D} = \begin{bmatrix} \nabla^2 & 0 & 0 & 0 \\ 0 & 1 & 0 & 0 \\ 0 & 0 & 1 & 0 \\ 0 & 0 & 0 & 1 \end{bmatrix} \tag{A5}$$

$$\mathcal{L}_0 = \begin{bmatrix} -\frac{1}{\mathrm{Re}}\partial_x^4 & 0 & 0 & 0 \\ 0 & -\frac{1}{\mathrm{Re}}\partial_x^2 & 0 & 0 \\ 0 & 0 & -\frac{1}{\mathrm{Rm}}\partial_x^2 & 0 \\ 0 & 0 & 0 & -\frac{1}{\mathrm{Rm}}\partial_x^2 \end{bmatrix} \tag{A6}$$

$$\mathcal{L}_1 = \begin{bmatrix} 0 & -2 & -\frac{2}{\beta}\partial_x^2 & 0 \\ (2-q)\Omega_0 & 0 & 0 & -\frac{2}{\beta} \\ -1 & 0 & 0 & 0 \\ 0 & -1 & q\Omega_0 & 0 \end{bmatrix} \tag{A7}$$

$$\mathcal{L}_2 = \begin{bmatrix} -2\frac{1}{\mathrm{Re}}\partial_x^2 & 0 & 0 & 0 \\ 0 & -\frac{1}{\mathrm{Re}} & 0 & 0 \\ 0 & 0 & -\frac{1}{\mathrm{Rm}} & 0 \\ 0 & 0 & 0 & -\frac{1}{\mathrm{Rm}} \end{bmatrix} \tag{A8}$$

$$\mathcal{L}_3 = \begin{bmatrix} 0 & 0 & -\frac{2}{\beta} & 0 \\ 0 & 0 & 0 & 0 \\ 0 & 0 & 0 & 0 \\ 0 & 0 & 0 & 0 \end{bmatrix} \tag{A9}$$

$$\mathcal{L}_4 = \begin{bmatrix} -\frac{1}{\mathrm{Re}} & 0 & 0 & 0 \\ 0 & 0 & 0 & 0 \\ 0 & 0 & 0 & 0 \\ 0 & 0 & 0 & 0 \end{bmatrix} \tag{A10}$$

$$\mathcal{G} = \begin{bmatrix} 0 & 0 & -\frac{2}{\beta}\partial_x^2 & 0 \\ 0 & 0 & 0 & -\frac{2}{\beta} \\ -1 & 0 & 0 & 0 \\ 0 & -1 & 0 & 0 \end{bmatrix} \tag{A11}$$

Once perturbed, the system is solved for successive orders of ϵ (Equations 18 - 20). $\mathcal{O}(\epsilon)$ is the linear system. At $\mathcal{O}(\epsilon^2)$, first-order MRI modes nonlinearly interact with themselves and with their complex conjugates, and so the term $\mathbf{N}_2$ in Equation 19 has the form

$$\mathbf{N}_2 = |\alpha|^2 \mathbf{N}_{20} + \alpha^2 \mathbf{N}_{22} e^{2ik_c z} \tag{A12}$$

(see Appendix B for the full form of $\mathbf{N}_{20}$ and $\mathbf{N}_{22}$).

Note that, following the notation of Umurhan et al. (2007b), the subscripts refer to ϵ order, z order, successively, such that $\mathbf{N}_{22}$ is the second-order nonlinear term which corresponds to $e^{2ik_c z}$ z-dependence.

Equation 19 is solved as three separate systems of equations, one for each possible z resonance:

$$\mathcal{L}\mathbf{V}_{20} = \mathbf{N}_{20} \tag{A13}$$

$$\mathcal{L}\mathbf{V}_{21} = -\widetilde{\mathcal{L}}_1\partial_Z\mathbf{V}_{11} \tag{A14}$$

$$\mathcal{L}\mathbf{V}_{22} = \mathbf{N}_{22} \tag{A15}$$

Finally, at $\mathcal{O}(\epsilon^3)$ we eliminate secular terms to close the system. Secular terms are terms which are resonant with the solution to the homogenous linear equation (Equation 18), and which cause the higher-order solutions to grow without bound. The solvability criterion we enforce to eliminate these terms is the vanishing of the inner product of the solution to the adjoint linear homogenous equation $\mathcal{L}^\dagger\mathbf{V}^\dagger = 0$ with the nonhomogenous terms in Equation 20, namely

$$\langle\mathbb{V}^\dagger|\mathcal{D}\mathbb{V}_{11}\rangle\partial_T\alpha + \langle\mathbb{V}^\dagger|\widetilde{\mathcal{G}}\mathbb{V}_{11}\rangle\alpha + \langle\mathbb{V}^\dagger|\widetilde{\mathcal{L}}_1\mathbb{V}_{21} + \widetilde{\mathcal{L}}_2\mathbb{V}_{11}\rangle\partial_Z^2\alpha = \langle\mathbb{V}^\dagger|\mathbf{N}_{31}\rangle\alpha|\alpha|^2. \tag{A16}$$

This solvability criterion derives from a corollary to the Fredholm Alternative (see Paper II for a formal definition). Equation A16 can be rewritten as Equation 21, the Ginzburg-Landau equation, where the coefficients are

$$b = \langle\mathbb{V}^\dagger|\widetilde{\mathcal{G}}\mathbb{V}_{11}\rangle/\langle\mathbb{V}^\dagger|\mathcal{D}\mathbb{V}_{11}\rangle, \tag{A17}$$

$$h = \langle\mathbb{V}^\dagger|\widetilde{\mathcal{L}}_1\mathbb{V}_{21} + \widetilde{\mathcal{L}}_2\mathbb{V}_{11}\rangle/\langle\mathbb{V}^\dagger|\mathcal{D}\mathbb{V}_{11}\rangle, \tag{A18}$$

and

$$c = \langle\mathbb{V}^\dagger|\mathbf{N}_{31}\rangle/\langle\mathbb{V}^\dagger|\mathcal{D}\mathbb{V}_{11}\rangle. \tag{A19}$$

We define the adjoint operator $\mathcal{L}^\dagger$ and solution $\mathbf{V}^\dagger$ as

$$\langle\mathbf{V}^\dagger|\mathcal{L}\mathbf{V}\rangle = \langle\mathcal{L}^\dagger\mathbf{V}^\dagger|\mathbf{V}\rangle, \tag{A20}$$

where the inner product is defined as

$$\langle\mathbf{V}^\dagger|\mathcal{L}\mathbf{V}\rangle = \frac{k_c}{2\pi}\int_{-\pi/k_c}^{\pi/k_c}\int_{x_1}^{x_2}\mathbf{V}^{\dagger *}\cdot\mathcal{L}\mathbf{V}\,\mathrm{d}x\mathrm{d}z. \tag{A21}$$

The solution to the adjoint homogenous equation has the form

$$\mathbf{V}^\dagger = \mathbb{V}^\dagger(x)e^{ik_cz} + c.c. \tag{A22}$$

As noted by URM07, a second amplitude equation for a spatially constant azimuthal magnetic field mode arises from the terms in the $\mathcal{O}(\epsilon^3)$ equation which contain no z dependence. This is a diffusion equation, so the neutral mode simply decays away.

B. EXPANSION OF NONLINEAR TERMS

At each order in our perturbation series, lower-order MRI modes nonlinearly interact. Thus there is a nonlinear term contribution at $\mathcal{O}(\epsilon^2)$ and $\mathcal{O}(\epsilon^3)$. Here we detail the form of these nonlinear terms.

The overall nonlinear contribution to our system, written as a vector $\mathbf{N}$ in Equation 13, is

$$\mathbf{N} = \epsilon^2\mathbf{N_2} + \epsilon^3\mathbf{N_3} + \mathcal{O}(\epsilon^4) \tag{B1}$$

where

$$N_2^{(\Psi)} = J(\Psi_1, \nabla^2\Psi_1) - \frac{2}{\beta}J(A_1, \nabla^2 A_1) \tag{B2}$$

$$N_2^{(u)} = J(\Psi_1, u_1) - \frac{2}{\beta}J(A_1, B_1) \tag{B3}$$

$$N_2^{(A)} = -J(A_1, \Psi_1) \tag{B4}$$

$$N_2^{(B)} = J(\Psi_1, B_1) - J(A_1, u_1) \tag{B5}$$

and

$$N_3^{(\Psi)} = J(\Psi_1, \nabla^2\Psi_2) - \frac{2}{\beta}J(A_1, \nabla^2 A_2) + J(\Psi_2, \nabla^2\Psi_1) - \frac{2}{\beta}J(A_2, \nabla^2 A_1) + 2J(\Psi_1, \partial_z\partial_Z\Psi_1)$$
$$- 2\frac{2}{\beta}J(A_1, \partial_z\partial_Z A_1) + \widetilde{J}(\Psi_1, \nabla^2\Psi_1) - \frac{2}{\beta}\widetilde{J}(A_1, \nabla^2 A_1) \tag{B6}$$

$$N_3^{(u)} = J(\Psi_1, u_2) + J(\Psi_2, u_1) + \widetilde{J}(\Psi_1, u_1) - \frac{2}{\beta}J(A_1, B_2) - \frac{2}{\beta}J(A_2, B_1) - \frac{2}{\beta}\widetilde{J}(A_1, B_1) \tag{B7}$$

$$N_3^{(A)} = -J(A_1, \Psi_2) - J(A_2, \Psi_1) - \widetilde{J}(A_1, \Psi_1) \tag{B8}$$

$$N_3^{(B)} = J(\Psi_1, B_2) + J(\Psi_2, B_1) + \widetilde{J}(\Psi_1, B_1) - J(A_1, u_2) - J(A_2, u_1) - \widetilde{J}(A_1, u_1). \tag{B9}$$

$\mathbf{N_2}$ and $\mathbf{N_3}$ expand to become

$$\mathbf{N_2} = \alpha^2\mathbb{N}_{22}e^{i2k_cz} + |\alpha|^2\,\mathbb{N}_{20} + c.c. \tag{B10}$$

and

$$\mathbf{N_3} = \alpha^3\mathbb{N}_{33}e^{i3k_cz} + \alpha\partial_Z\alpha\mathbb{N}_{32}e^{i2k_cz} + \alpha\,|\alpha|^2\,\mathbb{N}_{31}e^{ik_cz} + \alpha\partial_Z\beta\widetilde{\mathbb{N}}_{31}e^{ik_cz} + \alpha^*\partial_Z\alpha\mathbb{N}_{30} + c.c. \tag{B11}$$

The second order nonlinear terms are

$$N_{22}^{(\Psi)} = ik_c\Psi_{11} \cdot \left(\partial_x^3\Psi_{11} - k_c^2\partial_x\Psi_{11}\right) - \partial_x\Psi_{11} \cdot \left(ik_c\partial_x^2\Psi_{11} - ik_c^3\Psi_{11}\right)$$
$$+ \frac{2}{\beta}\partial_x A_{11} \cdot \left(ik_c\partial_x^2 A_{11} - ik_c^3 A_{11}\right) - \frac{2}{\beta}ik_c A_{11} \cdot \left(\partial_x^3 A_{11} - k_c^2\partial_x A_{11}\right) \tag{B12}$$

$$N_{22}^{(u)} = ik_c\Psi_{11} \cdot \partial_x u_{11} - \partial_x\Psi_{11} \cdot ik_c u_{11} - \frac{2}{\beta}ik_c A_{11} \cdot \partial_x B_{11} + \frac{2}{\beta}\partial_x A_{11} \cdot ik_c B_{11} \tag{B13}$$

$$N_{22}^{(A)} = -ik_c A_{11} \cdot \partial_x\Psi_{11} + \partial_x A_{11} \cdot ik_c\Psi_{11} \tag{B14}$$

$$N_{22}^{(B)} = ik_c\Psi_{11} \cdot \partial_x B_{11} - \partial_x\Psi_{11} \cdot ik_c B_{11} - ik_c A_{11} \cdot \partial_x u_{11} + \partial_x A_{11} \cdot ik_c u_{11} \tag{B15}$$

$$N_{20}^{(\Psi)} = ik_c\Psi_{11} \cdot \left(\partial_x^3\Psi_{11}^* - k_c^2\partial_x\Psi_{11}^*\right) - \partial_x\Psi_{11} \cdot \left(ik_c^3\Psi_{11}^* - ik_c\partial_x^2\Psi_{11}^*\right)$$
$$+ \frac{2}{\beta}\partial_x A_{11} \cdot \left(ik_c^3 A_{11}^* - ik_c\partial_x^2 A_{11}^*\right) - \frac{2}{\beta}ik_c A_{11} \cdot \left(\partial_x^3 A_{11}^* - k_c^2\partial_x A_{11}^*\right) \tag{B16}$$

$$N_{20}^{(u)} = ik_c\Psi_{11} \cdot \partial_x u_{11}^* + \partial_x\Psi_{11} \cdot ik_c u_{11}^* - \frac{2}{\beta}ik_c A_{11} \cdot \partial_x B_{11}^* - \frac{2}{\beta}\partial_x A_{11} \cdot ik_c B_{11}^* \tag{B17}$$

$$N_{20}^{(A)} = -ik_c A_{11} \cdot \partial_x\Psi_{11}^* - \partial_x A_{11} \cdot ik_c\Psi_{11}^* \tag{B18}$$

$$N_{20}^{(B)} = ik_c\Psi_{11} \cdot \partial_x B_{11}^* + \partial_x\Psi_{11} \cdot ik_c B_{11}^* - ik_c A_{11} \cdot \partial_x u_{11}^* - \partial_x A_{11} \cdot ik_c u_{11}^* \tag{B19}$$

and the third order nonlinear terms become

$$
\begin{aligned}
N_{31}^{(\Psi)} =\ & ik_c \left(\Psi_{11} \cdot \partial_x^3 \Psi_{20}\right) + ik_c \left(\Psi_{11} \cdot \partial_x^3 \Psi_{20}^*\right) - ik_c \left(\Psi_{11}^* \cdot \partial_x^3 \Psi_{22}\right) - i2k_c \left(\partial_x \Psi_{11}^* \cdot \partial_x^2 \Psi_{22}\right) \\
& + i8k_c^3 \left(\partial_x \Psi_{11}^* \cdot \Psi_{22}\right) + i4k_c^3 \left(\Psi_{11}^* \cdot \partial_x \Psi_{22}\right) + \frac{2}{\beta} \left[-ik_c \left(A_{11} \cdot \partial^3 A_{20}\right) - ik_c \left(A_{11} \cdot \partial_x^3 A_{20}^*\right)\right] \\
& + \frac{2}{\beta} \left[ik_c \left(A_{11}^* \cdot \partial_x^3 A_{22}\right) + i2k_c \left(\partial_x A_{11}^* \cdot \partial_x^2 A_{22}\right) - i8k_c^3 \left(\partial_x A_{11}^* \cdot A_{22}\right) - i4k_c^3 \left(A_{11}^* \cdot \partial_x A_{22}\right)\right] \\
& + i2k_c \left(\Psi_{22} \cdot \partial_x^3 \Psi_{11}^*\right) - i2k_c^3 \left(\Psi_{22} \cdot \partial_x \Psi_{11}^*\right) - ik_c \left(\partial_x \Psi_{20} \cdot \partial_x^2 \Psi_{11}\right) + ik_c \left(\partial_x \Psi_{22} \cdot \partial_x^2 \Psi_{11}^*\right) \\
& - ik_c \left(\partial_x \Psi_{20}^* \cdot \partial_x^2 \Psi_{11}\right) + ik_c^3 \left(\partial_x \Psi_{20} \cdot \Psi_{11}\right) + ik_c^3 \left(\partial_x \Psi_{20}^* \cdot \Psi_{11}\right) - ik_c^3 \left(\partial_x \Psi_{22} \cdot \Psi_{11}^*\right) \\
& + \frac{2}{\beta} \left[-i2k_c \left(A_{22} \cdot \partial_x^3 A_{11}^*\right) + i2k_c^3 \left(A_{22} \cdot \partial_x A_{11}^*\right) + ik_c \left(\partial_x A_{20} \cdot \partial_x^2 A_{11}\right) - ik_c \left(\partial_x A_{22} \cdot \partial_x^2 A_{11}^*\right)\right] \\
& + \frac{2}{\beta} \left[ik_c \left(\partial_x A_{20}^* \cdot \partial_x^2 A_{11}\right) - ik_c^3 \left(\partial_x A_{20} \cdot A_{11}\right) - ik_c^3 \left(\partial_x A_{20}^* \cdot A_{11}\right) + ik_c^3 \left(\partial_x A_{22} \cdot A_{11}^*\right)\right]
\end{aligned} \tag{B20}
$$

$$
\begin{aligned}
N_{31}^{(u)} =\ & ik_c \left(\Psi_{11} \cdot \partial_x u_{20}\right) + ik_c \left(\Psi_{11} \cdot \partial_x u_{20}^*\right) - ik_c \left(\Psi_{11}^* \cdot \partial_x u_{22}\right) - i2k_c \left(\partial_x \Psi_{11}^* \cdot u_{22}\right) \\
& - ik_c \left(u_{11} \cdot \partial_x \Psi_{20}\right) - ik_c \left(u_{11} \cdot \partial_x \Psi_{20}^*\right) + ik_c \left(u_{11}^* \cdot \partial_x \Psi_{22}\right) + i2k_c \left(\partial_x u_{11}^* \cdot \Psi_{22}\right) \\
& + \frac{2}{\beta} \left[-ik_c \left(A_{11} \cdot \partial_x B_{20}\right) - ik_c \left(A_{11} \cdot \partial_x B_{20}^*\right) + ik_c \left(A_{11}^* \cdot \partial_x B_{22}\right) + i2k_c \left(\partial_x A_{11}^* \cdot B_{22}\right)\right] \\
& + \frac{2}{\beta} \left[ik_c \left(B_{11} \cdot \partial_x A_{20}\right) + ik_c \left(B_{11} \cdot \partial_x A_{20}^*\right) - ik_c \left(B_{11}^* \cdot \partial_x A_{20}\right) - i2k_c \left(\partial_x B_{11}^* \cdot A_{22}\right)\right]
\end{aligned} \tag{B21}
$$

$$
\begin{aligned}
N_{31}^{(A)} =\ & -ik_c \left(A_{11} \cdot \partial_x \Psi_{20}\right) - ik_c \left(A_{11} \cdot \partial_x \Psi_{20}^*\right) + ik_c \left(A_{11}^* \cdot \partial_x \Psi_{22}\right) + i2k_c \left(\partial_x A_{11}^* \cdot \Psi_{22}\right) \\
& + ik_c \left(\Psi_{11} \cdot \partial_x A_{20}\right) + ik_c \left(\Psi_{11} \cdot \partial_x A_{20}^*\right) - ik_c \left(\Psi_{11}^* \cdot \partial_x A_{22}\right) - i2k_c \left(\partial_x \Psi_{11}^* \cdot A_{22}\right)
\end{aligned} \tag{B22}
$$

$$
\begin{aligned}
N_{31}^{(B)} =\ & ik_c \left(\Psi_{11} \cdot \partial_x B_{20}\right) + ik_c \left(\Psi_{11} \cdot \partial_x B_{20}^*\right) - ik_c \left(\Psi_{11}^* \cdot \partial_x B_{22}\right) - i2k_c \left(\partial_x \Psi_{11}^* \cdot B_{22}\right) \\
& - ik_c \left(B_{11} \cdot \partial_x \Psi_{20}\right) - ik_c \left(B_{11} \cdot \partial_x \Psi_{20}^*\right) + ik_c \left(B_{11}^* \cdot \partial_x \Psi_{22}\right) + i2k_c \left(\partial_x B_{11}^* \cdot \Psi_{22}\right) \\
& - ik_c \left(A_{11} \cdot \partial_x u_{20}\right) - ik_c \left(A_{11} \cdot \partial_x u_{20}^*\right) + ik_c \left(A_{11}^* \cdot \partial_x u_{22}\right) + i2k_c \left(\partial_x A_{11}^* \cdot u_{22}\right) \\
& ik_c \left(u_{11} \cdot \partial_x A_{20}\right) + ik_c \left(u_{11} \cdot \partial_x A_{20}^*\right) - ik_c \left(u_{11}^* \cdot \partial_x A_{22}\right) - i2k_c \left(\partial_x u_{11}^* \cdot A_{22}\right)
\end{aligned} \tag{B23}
$$

C. LINEAR DISPERSION RELATION

The linear dispersion relation, which determines the variable scalings in the multiple scales analysis. This relation is found by perturbing the linear system (Equation 18) with a small perturbation of the form $e^{\sigma t + ik_x x + ik_z z}$. Note that the spatial eigenvalues appear as k_z^2 and k_x^2 at lowest order.

$$
\begin{aligned}
& \frac{B_0^4 k_x^2 k_z^4}{16\pi^2} + \frac{B_0^4 k_z^6}{16\pi^2} - \frac{B_0^2 \Omega_0 k_z^4 q}{2\pi} - 2\Omega_0 k_z^2 q \sigma^2 - \frac{4\sigma}{\text{Rm}} \Omega_0 k_x^2 k_z^2 q - \frac{4\sigma}{\text{Rm}} \Omega_0 k_z^4 q - \frac{2\Omega_0}{\text{Rm}^2} k_x^4 k_z^2 q - \frac{4\Omega_0}{\text{Rm}^2} k_x^2 k_z^4 q - \frac{2\Omega_0}{\text{Rm}^2} k_z^6 q \\
& - k_x^2 \sigma^4 - k_z^2 \sigma^4 + 4k_z^2 \sigma^2 - \frac{2\sigma^3}{\text{Rm}} k_x^4 - \frac{4\sigma^3}{\text{Rm}} k_x^2 k_z^2 + \frac{8\sigma}{\text{Rm}} k_x^2 k_z^2 - \frac{2\sigma^3}{\text{Rm}} k_z^4 + \frac{8\sigma}{\text{Rm}} k_z^4 - \frac{k_x^6 \sigma^2}{\text{Rm}^2} - \frac{3\sigma^2}{\text{Rm}^2} k_x^4 k_z^2 + \frac{4k_x^4}{\text{Rm}^2} k_z^2 \\
& - \frac{3\sigma^2}{\text{Rm}^2} k_x^2 k_z^4 + \frac{8k_x^2}{\text{Rm}^2} k_z^4 - \frac{k_z^6 \sigma^2}{\text{Rm}^2} + \frac{4k_z^6}{\text{Rm}^2} - \frac{2\sigma^3}{\text{Re}} k_x^4 - \frac{4\sigma^3}{\text{Re}} k_x^2 k_z^2 - \frac{2\sigma^3}{\text{Re}} k_z^4 - \frac{4k_x^6 \sigma^2}{\text{ReRm}} - \frac{12k_x^4 k_z^2 \sigma^2}{\text{ReRm}} - \frac{12k_x^2 k_z^4 \sigma^2}{\text{ReRm}} \\
& - \frac{4k_z^6 \sigma^2}{\text{ReRm}} - \frac{2k_x^8 \sigma}{\text{ReRm}^2} - \frac{8k_x^6 k_z^2 \sigma}{\text{ReRm}^2} - \frac{12k_x^4 k_z^4 \sigma}{\text{ReRm}^2} - \frac{8k_x^2 k_z^6 \sigma}{\text{ReRm}^2} - \frac{2k_z^8 \sigma}{\text{ReRm}^2} - \frac{k_x^6 \sigma^2}{\text{Re}^2} - \frac{3\sigma^2}{\text{Re}^2} k_x^4 k_z^2 - \frac{3\sigma^2}{\text{Re}^2} k_x^2 k_z^4 - \frac{k_z^6 \sigma^2}{\text{Re}^2} \\
& - \frac{2k_x^8 \sigma}{\text{Re}^2 \text{Rm}} - \frac{8k_x^6 k_z^2 \sigma}{\text{Re}^2 \text{Rm}} - \frac{12k_x^4 k_z^4 \sigma}{\text{Re}^2 \text{Rm}} - \frac{8k_x^2 k_z^6 \sigma}{\text{Re}^2 \text{Rm}} - \frac{2k_z^8 \sigma}{\text{Re}^2 \text{Rm}} - \frac{k_x^{10}}{\text{Re}^2 \text{Rm}^2} - \frac{5k_x^8 k_z^2}{\text{Re}^2 \text{Rm}^2} - \frac{10k_x^6 k_z^4}{\text{Re}^2 \text{Rm}^2} - \frac{10k_x^4 k_z^6}{\text{Re}^2 \text{Rm}^2} \\
& - \frac{5k_x^2 k_z^8}{\text{Re}^2 \text{Rm}^2} - \frac{k_z^{10}}{\text{Re}^2 \text{Rm}^2} = 0
\end{aligned} \tag{C1}
$$

REFERENCES

Bai, X.-N. 2015, ApJ, 798, 84

Balbus, S A and Hawley, J F, 1991, The Astrophysical Journal, 376, 214

Bender, C. M., & Orszag, S. A. 1978, Advanced Mathematical Methods for Scientists and Engineers, New York: McGraw-Hill, 1978,

Boyd, J P, 2001, Chebyshev and Fourier Spectral Methods, New York, Dover

Chandrasekhar, S. 1960, Proceedings of the National Academy of Sciences of the United States of America, 46, 253

Clark, S.E. and Oishi, J.S., 2016, submitted

Ebrahimi, F., Prager, S.C., Schnack, D.D, 2009, ApJ 698, 233

Goodman, J, Xu, G, 1994, ApJ, 432, 213

Hawley, J. F., Guan, X., & Krolik, J. H. 2011, ApJ, 738, 84

Hoyle, R. 2006, Pattern Formation, by Rebecca Hoyle, pp. 432. Cambridge University Press, March 2006. ISBN-10: 0521817501. ISBN-13: 9780521817509, 432

Knobloch, E, Julien K, 2005, Physics of Fluids, 17, 094106

Latter, H.N., Fromang, S., & Faure, J., 2015, MNRAS 453, 3257

Latter, H.N., Fromang, S., & Gressel, O., 2010, MNRAS 406, 848

Newell, A.C. & Whitehead, J.A. 1969, JFM 38, 279N

Parkin, E. R. 2014, MNRAS, 438, 2513

Parkin, E. R., & Bicknell, G. V. 2013, MNRAS, 435, 2281

Pessah, M. E., 2010, ApJ, 716, 1012

Pessah, M. E., & Goodman, J., 2009, ApJ 698, L72

Rembiasz, T., Obergaulinger, M., Cerdá-Durán, P., Müller, E., & Aloy, M.A., 2016, MNRAS 456, 3782

Schnittman, J. D., Krolik, J. H., & Noble, S. C. 2013, ApJ, 769, 156

Shakura, N I and Sunyaev, R A, Astronomy & Astrophysics, 1973, 24, 337

Umurhan, O M, Regev, O, Menou, K, 2007, Phys. Rev. Letters, 98, 034501

Umurhan, O M, Regev, O, Menou, K, 2007, Phys. Rev. E, 76, 036310

Vasil, G. M. 2015, RSPSA 471, 20140699

Velikhov, E. P., 1959, Sov. Phys. JETP 36, 995.

Wheeler, J. C., Kagan, D., & Chatzopoulos, E. 2015, ApJ, 799, 85